

## Probing topological Floquet states in $\text{WSe}_2$ using circular dichroism in time- and angle-resolved photoemission spectroscopy

Michael Schüler <sup>1</sup>✉ & Samuel Beaulieu<sup>2</sup>

Observing signatures of light-induced topological Floquet states in materials has been shown to be very challenging. Angle-resolved photoemission spectroscopy (ARPES) is well suited for the investigation of Floquet physics, as it allows to directly probe the dressed electronic states of driven solids. Depending on the system, scattering and decoherence can play an important role, hampering the emergence of Floquet states. Another challenge is to disentangle Floquet side bands from laser-assisted photoemission (LAPE), since both lead to similar signatures in ARPES spectra. Here, we investigate the emergence of Floquet state in the transition metal dichalcogenide  $2H\text{-WSe}_2$ , one of the most promising systems for observing Floquet physics. We discuss how the topological Floquet state manifests in characteristic features in the circular dichroism in photoelectron angular distributions (CDAD) that is determined by the transient band structure modifications and the associated texture of the orbital angular momentum. Combining highly accurate modeling of the photoemission matrix elements with an *ab initio* description of the light-matter interaction, we investigate regimes which can be realized in current state-of-the-art experimental setups. The predicted features are robust against scattering effects and are expected to be observed in forthcoming experiments.

<sup>1</sup>Condensed Matter Theory Group, Paul Scherrer Institute, CH-5232 Villigen PSI, Switzerland. <sup>2</sup>Université de Bordeaux-CNRS-CEA, CELIA, UMR5107, F33405 Talence, France. ✉email: [michael.schueler@psi.ch](mailto:michael.schueler@psi.ch)

Controlling properties of quantum materials by tailored light is at the forefront of condensed matter physics<sup>1,2</sup> due to recent advances of ultrafast laser technologies. In particular, manipulating the electronic structure's topology and creating on-demand topological properties—theoretically predicted in ref. 3—is one of the most fundamental goals of the field. The key idea is that periodically driven solids (described by Floquet theory) form effective bands that correspond to a topologically non-trivial state. While countless theoretical proposals exist, direct experimental observations of Floquet physics are scarce. The first experiments confirming the Floquet hallmarks—emergence of side bands and gap openings—have been performed on the surface of Bi<sub>2</sub>Se<sub>3</sub><sup>4,5</sup> using time- and angle-resolved photoemission spectroscopy (trARPES). Observing Floquet features in graphene, following the original proposal from ref. 3, has proven difficult, as the interplay of decoherence<sup>6,7</sup> and scattering effects<sup>8–10</sup> is adversarial to the formation of Floquet states. Indeed, it has been concluded that Floquet-Bloch states cannot emerge if the scattering time of the electrons is shorter than or comparable to the period of the driving field<sup>10</sup>. Furthermore, laser-assisted photoemission (LAPE)<sup>11</sup> often overshadows the Floquet side bands<sup>5,12</sup>. To enhance the typically weak photodressing of the electronic bands, using intense low-frequency pump pulses emerged as a new direction<sup>10,13</sup> to investigate Floquet physics in real systems. However, in this regime, scattering effects are becoming more pronounced: if the duration of the optical cycles is long compared to the decoherence time, the emergence of Floquet features is suppressed. Alternatively, evidencing the Floquet-topological state in light-driven graphene via transport measurements<sup>14,15</sup> is a promising route, albeit the manifestation of the topology in ref. 14 is far from clear<sup>7</sup>.

trARPES is the most direct experimental technique to access the electronic structure and occupations in photodressed solids<sup>16–19</sup>. However, instead of focusing on the spectral features of photodressed band structure alone, mapping out properties of the associated Bloch wave-functions would yield a new level of insight. Information on the Bloch wave-function manifests in the complex photoemission matrix elements (interference effects and anisotropy of the photoemission intensity<sup>20,21</sup>), leading to (linear and circular) dichroism in the ARPES spectrum. In static ARPES, the circular dichroism in the photoelectron angular distributions (CDAD) has been proven to be a powerful tool to map out pseudospin properties<sup>22,23</sup>, helical spin textures<sup>24–26</sup>, high-symmetry planes<sup>27</sup> in 3D reciprocal space, and Berry curvature<sup>28–32</sup>. The sensitivity of the CDAD to topological properties is due to the intimate connection between Berry curvature and orbital angular momentum (OAM)<sup>33</sup>. This link provides a new avenue for observing light-induced topology from features in the CDAD in trARPES.

While graphene is the paradigmatic material for the emergence of light-induced topological states<sup>3,8</sup>, complications like the sample size and/or quality as well as very fast electronic scattering time, render such experimental demonstration very difficult<sup>10</sup>. At variance, Floquet physics has been predicted by first-principle calculations<sup>34</sup> and has been observed experimentally in transition metal dichalcogenides (TMDCs)<sup>10,35</sup>. Furthermore, as predicted in ref. 36, a Floquet-Chern insulating state can be realized in the conduction band manifold. This raises the question: can we use CDAD in time-resolved ARPES to directly probe the light-induced topological state in driven TMDCs?

In this work, we address this fundamental question by predictive simulations. We are motivated by recent experimental progress that allows to perform XUV-trARPES measurements with femtosecond time resolution<sup>19,37–44</sup>. Achieving circularly polarized XUV pulses at hundreds of kilohertz repetition-rate is the key technical challenge for measuring transient CDAD across the entire Brillouin zone. While this was not demonstrated yet, all

the technological building blocks (high-repetition-rate XUV source and XUV quarter-wave plate<sup>45–48</sup>) allowing to performed such experiments are available and are currently being put together by some experimental groups (including one of the authors). The purpose of this paper is to predict the Floquet features in laser-driven TMDC and the associated CDAD, under conditions that are directly compatible with trARPES setups.

Our main finding is that the emergence of Floquet side bands is accompanied by the formation of specific orbital textures with locally non-trivial topological characters, giving rise to a distinct CDAD signal. We also show that the dichroic signal is robust against dissipation and should be observable in a wide range of parameters. We use atomic units (a.u.) unless stated otherwise.

## Results

Analogous to the previous experiments<sup>49,50</sup> we consider the surface of bulk 2H-WSe<sub>2</sub>. To study the transient photodressing effects, we consider the following pump-probe setup. A relatively strong, circularly polarized pump pulse (typical peak intensity in the range of  $I_0 \sim 10^{11}$  W/cm<sup>2</sup>—reached using realistic fluences of 1 mJ/cm<sup>2</sup> using 10 fs pulse and of 30 mJ/cm<sup>2</sup> for 300 fs pulse, which spans the typical pump pulse duration range of trARPES setups) induces Floquet features in the electronic structure, which are probed by circularly polarized XUV probe pulses (see Fig. 1a). Similar to typical ARPES setups using time-of-flight detector allowing to record the photoemission signal in the entire Brillouin zone within a single measurement<sup>44,49,51–53</sup>, we assume an incidence angle of  $\theta = 65^\circ$  for the propagation direction of the XUV probe, as illustrated in Fig. 1b. Varying the time delay  $\Delta t$  between the pump and probe pulses allows observing the transient build-up of the photodressing effects. However, the Floquet features in the trARPES spectrum are maximized for the probe pulse centered at the peak of the envelope of the pump pulse, which is the regime we focus on in this work. In a typical setup, both the pump and the probe pulse impinge under the same angle  $\theta$ . However, for simplicity we take the circular polarization of the pump to be in the  $x$ - $y$  plane, which can effectively be implemented by generated elliptically polarized pump pulses propagating collinearly with the probe pulse. The out-of-plane component does not play an important role for 2H-WSe<sub>2</sub> due to the weak coupling of between layers. The results presented in this work are also robust against lifting this restriction.

**Model and light-matter coupling.** As discussed e.g. in ref. 49, in the above described experimental condition, only the top-most layer of the bulk sample contributes notably to the photoemission

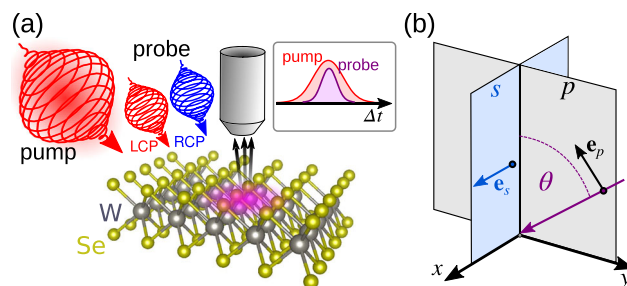


**Fig. 1 Sketch of the setup.** **a** A left-hand circularly polarized (LCP) or right-hand circularly polarized (RCP) pump pulse transiently dresses the electronic structure of bulk 2H-WSe<sub>2</sub>, which is probed by a circularly polarized femtosecond extreme ultraviolet (XUV) pulse. The probe pulse is centered at time delay  $\Delta t = 0$  with respect to the peak of the pump pulse. **b** Geometry of the simulated experiment: the propagation direction of the probe pulse is in the  $p$  plane ( $x$ - $y$  plane), rotated by an angle of  $\theta = 65^\circ$  with respect to the  $z$  axis. The  $s$  plane is along the  $x$  axis.

signal. Hence, for our theoretical investigations, we model the system by a monolayer of WSe<sub>2</sub>, which simplifies the theory considerably while retaining the relevant physics. The electronic properties and associated photoemission intensities in the vicinity of the K, K' valleys are well captured by a monolayer; small corrections to the photoemission properties due to bilayer interference—as discussed in ref. 54—are built into the theory by fitting to experimental data, as explained below in the method section.

The electronic structure is described by the first-principle Wannier model from ref. 55, which comprises the Se *p* orbitals and W *d* orbitals (11 orbitals in total). In Wannier presentation, the Bloch states of band  $\alpha$  are given by

$$\psi_{\mathbf{k}\alpha}(\mathbf{r}) = \frac{1}{\sqrt{N}} \sum_{\mathbf{R},j} e^{i\mathbf{k}\cdot\mathbf{R}} C_{j\alpha}(\mathbf{k}) \phi_j(\mathbf{r} - \mathbf{R}) \equiv \sum_j C_{j\alpha}(\mathbf{k}) \phi_{kj}(\mathbf{r}), \quad (1)$$

where  $\mathbf{R}$  runs over all  $N$  lattice sites;  $\phi_j(\mathbf{r})$  denote the Wannier orbitals. The coefficients  $C_{j\alpha}(\mathbf{k})$  determine the complex superposition of the orbitals and thus the orbital texture. To describe the photoemission by the XUV probe pulse, we need the photoemission matrix elements  $M_\alpha(\mathbf{k}, E) = \langle \mathbf{k}, E | \mathbf{e} \cdot \hat{\mathbf{p}} | \psi_{\mathbf{k}\alpha} \rangle$  ( $\hat{\mathbf{p}}$  denotes the momentum operator) with respect to the initial Bloch state and the final state determined by the in-plane momentum  $\mathbf{k}$  and the energy of the outgoing photoelectron  $E$ . Matrix-element effects encode the orbital texture and the orbital angular momentum of the Bloch states. For our simulations to be predictive, an accurate model of matrix elements is thus crucial. We construct such a model by directly fitting calculated photoemission intensities to experimental data, which contains characteristic signal modulation due to matrix-element effects. The most pronounced feature close to the valence band maximum (VBM) is the so-called dark corridor, i.e. the suppression of intensity along the edges of the Brillouin zone. The dark corridor is directly related to the interference of the relevant orbitals close to the VBM<sup>49,54</sup> and is very sensitive to both the underlying orbital character  $\phi_j(\mathbf{r})$  and their relative phase<sup>50</sup>. Therefore, a model that contains the correct orbital symmetries and reproduces the orientation of dark corridors in the Brillouin zone contains all the relevant phase information ingredients to predict spectra for both linear and circular polarization<sup>50</sup>. We construct such a model from the ansatz

$$M_\alpha(\mathbf{k}, E) = \sum_j C_{j\alpha}(\mathbf{k}) e^{i\gamma_j} M_j^{(\text{at})}(\mathbf{k}, E), \quad (2)$$

where  $M_j^{(\text{at})}(\mathbf{k}, E)$  denote the matrix elements with respect to the Wannier orbitals, calculated similarly as in atomic physics, while  $\gamma_j$  are additional phase shifts that account for final state effects. We have fitted the phases  $\gamma_j$  and the few parameters entering  $M_j^{(\text{at})}(\mathbf{k}, E)$  to experimental spectra from ref. 50 for both *s* and *p* polarized light (see methods section Supplementary Note 1 for details and the explicit comparison).

The Wannier representation Eq. (1) also provides a direct path to computing the light-matter coupling matrix elements that allow us to incorporate the pump field in a first-principle fashion<sup>55</sup>. Here we adopt the velocity gauge in which the time-dependent Hamiltonian (including the pump pulse only) is given by

$$H_{\alpha\alpha'}(\mathbf{k}, t) = \left( \varepsilon_\alpha(\mathbf{k}) + \frac{\mathbf{A}_p(t)^2}{2} \right) \delta_{\alpha\alpha'} - \mathbf{A}_p(t) \cdot \mathbf{v}_{\alpha\alpha'}(\mathbf{k}), \quad (3)$$

where  $\varepsilon_\alpha(\mathbf{k})$  is the band energy of corresponding the Bloch state, while  $\mathbf{v}_{\alpha\alpha'}(\mathbf{k}) = \langle \psi_{\mathbf{k}\alpha} | \hat{\mathbf{p}} | \psi_{\mathbf{k}\alpha'} \rangle$  are the matrix elements of the momentum operator  $\hat{\mathbf{p}}$ , known as the velocity matrix elements. The pump pulse is described by the vector potential  $\mathbf{A}_p(t)$  within the dipole approximation. The light-matter coupling entering

Eq. (3) accounts for intra- and inter-orbital transitions on equal footing. Furthermore, as opposed to the standard Peierls substitution, the calculation of the trARPES signal including photoemission matrix elements is straightforward<sup>56</sup>.

To calculate pump-probe ARPES intensities, we combine the light-matter coupling entering the Hamiltonian Eq. (3) and the photoemission matrix elements Eq. (2) with the nonequilibrium steady-state (NESS) approach. For a sufficiently long pump pulse, the trARPES signal for the probe pulse at the center of the pump can be described by the Floquet bands calculated from a purely time-periodic Hamiltonian. Due to electron-electron and electron-phonon scattering, the excited states reach a quasi-thermal state, thus determining the transient occupation of the Floquet bands<sup>57</sup>. In this regime, the NESS approach yields a realistic model for the trARPES signal<sup>8</sup>. The steady state reached by the dynamical balance of absorption and a generic type of dissipation is modeled by assuming that the monolayer WSe<sub>2</sub> is coupled to a wide-band thermalizing bath, while the excitation is induced by a time-periodic vector potential  $\mathbf{A}_p(t) = \mathbf{A}_0 \sin(\omega_p t)$ ,  $\omega_p = 2\pi/T_p$ . From these ingredients, we compute the lesser Green's function  $G_{\alpha\alpha'}^<(\mathbf{k}, t, t')$  within the NESS formalism (see methods section). Assuming a sufficiently long probe pulse, the trARPES signal is then obtained<sup>56,58</sup> from

$$I(\mathbf{k}, E) \propto \text{Im} \sum_{\alpha\alpha'} M_\alpha(\mathbf{k}, E) G_{\alpha\alpha'}^<(\mathbf{k}, \omega_{\text{pr}} - E) M_{\alpha'}^*(\mathbf{k}, E), \quad (4)$$

where

$$G_{\alpha\alpha'}^<(\mathbf{k}, \omega) = \frac{1}{T_p} \int_0^{T_p} dt_{\text{av}} \int_{-\infty}^{\infty} dt_{\text{rel}} e^{i\omega t_{\text{rel}}} \times G_{\alpha\alpha'}^<\left(t_{\text{av}} + \frac{t_{\text{rel}}}{2}, t_{\text{av}} - \frac{t_{\text{rel}}}{2}\right) \quad (5)$$

and  $\omega_{\text{pr}}$  denotes the frequency of the probe pulse. The lesser Green's function  $G_{\alpha\alpha'}^<(\mathbf{k}, \omega)$  contains both the information on the spectrum and the occupation. If we are only interested in the spectrum, we can compute the retarded Green's function  $G_{\alpha\alpha'}^R(\mathbf{k}, t, t')$ , which is transformed to frequency space by a direct analog of Eq. (5).

The only parameters of the NESS approach originate from the bath, which is characterized by a coupling strength  $\Gamma$  (which also determines the energy resolution) and an effective temperature  $T_{\text{eff}}$ . Computing the Green's function Eq. (5) in the presence of the bath determines the occupation of the excited states and the side-band intensity. We choose typical values for the bath temperature  $T_{\text{eff}} \sim 10^4 \text{K}$ , which yield realistic pump-probe photoemission spectra as discussed in ref. 8. Note that  $T_{\text{eff}}$  is different from the electronic temperature of WSe<sub>2</sub>, which is of the order of  $10^3 \text{K}$ .

**Orbital character and circular dichroism.** Before presenting the pump-probe spectra, it is instructive to discuss the orbital character of the relevant bands in equilibrium. The Bloch state of top valence band close to the VBM is dominated by the W  $d_{z^2}$ ,  $d_{xy}$  and  $d_{x^2-y^2}$  orbitals, which form magnetic states at the K, K' points. Therefore, it is convenient to work in the magnetic basis  $j \rightarrow \ell, m$ , where  $\ell, m$  correspond to complex spherical harmonics. In this basis, the Bloch state in the vicinity of the VBM is given by  $|\psi_{\mathbf{k}\alpha}^{K,K'}\rangle \approx [C_{2,0}(\mathbf{k})|\varphi_{\mathbf{k},2,0}\rangle + C_{2,\pm 2}(\mathbf{k})|\varphi_{\mathbf{k},2,\pm 2}\rangle] \otimes |\uparrow, \downarrow\rangle$ , where  $|\varphi_{\mathbf{k},2,0}\rangle$  ( $|\varphi_{\mathbf{k},2,\pm 2}\rangle$ ) denotes a Bloch state with  $d_{z^2}$  ( $d_{\pm 2} = (d_{x^2-y^2} \pm d_{xy})/\sqrt{2}$ ) orbitals localized at the W sites only. The orbital angular momentum (OAM) of a given Bloch state is reversed by rotating the crystal by  $60^\circ$ , which swaps  $K \leftrightarrow K'$  (see illustration in Fig. 2a). Hence, the rotation operation  $R_{60^\circ}$  is equivalent to a time-reversal operation<sup>49</sup>.

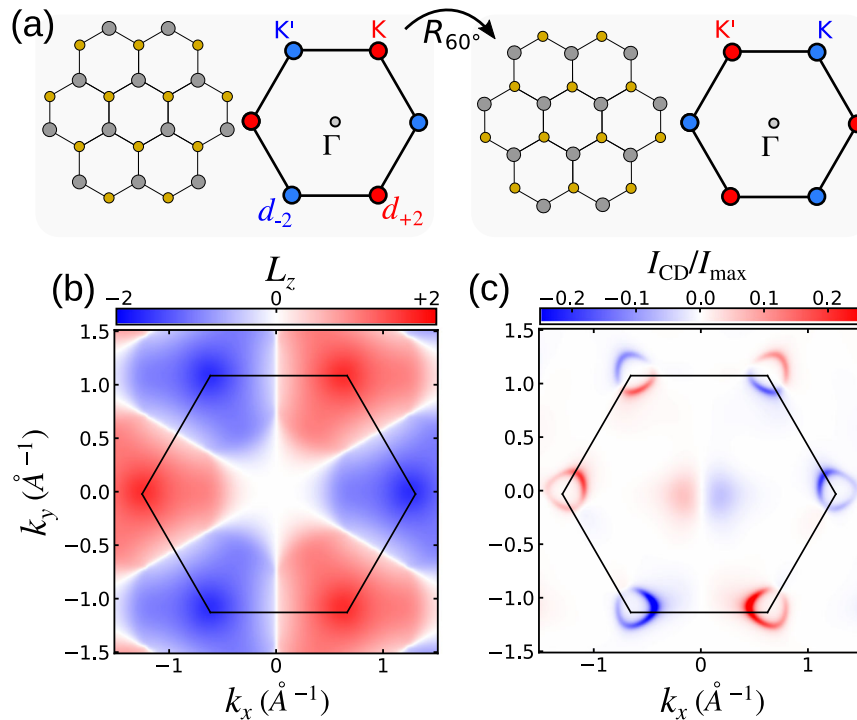


**Fig. 2 Orbital angular momentum and circular dichroism.** **a** Top view of the WSe<sub>2</sub> monolayer and sketch of the first Brillouin zone. Upon rotating the crystal by 60°, the dominant orbital character at K (K') reverse from the magnetic state  $d_{+2}$  ( $d_{-2}$ ) to  $d_{-2}$  ( $d_{+2}$ ), thus emulating the time-reversal operation. **b** Out-of-plane component of the orbital angular momentum  $L_z$  of the top valence band. The value of  $L_z$  is represented by the color as given by the color bar. **c** Calculated circular dichroism  $I_{CD}(\mathbf{k}, E) = I_{LCP}(\mathbf{k}, E) - I_{RCP}(\mathbf{k}, E)$  (LCP/RCP: left/right-hand circularly polarized) at binding energy  $E - E_{VBM} = -0.215$  eV for the orientation on the left-hand side of **(a)**. Positive (negative) values are indicated by red (blue) color as given by the color bar above. The circular dichroism for the rotated crystal orientation is qualitatively similar. The probe pulse is coming from above.

The OAM of the Bloch state can directly be accessed by circularly polarized probes. In particular, the OAM is reflected in circular dichroism in photoelectron angular distributions<sup>28–32</sup>, which can be understood intuitively by considering both the helicity of light and the self-rotation of the Bloch states<sup>33</sup>. In Fig. 2b we show the  $z$  component of the OAM of the top valence band, which qualitatively aligns with the texture of the  $d_{\pm 2}$  orbitals. How exactly the OAM and the circular dichroism are related quantitatively depends on details of the experimental geometry and the photon energy. Here we consider the geometry sketched in Fig. 1b. In this setup, left/right-hand circular polarized (LCP/RCP) light is defined by the polarization vector  $\mathbf{e}_{LCP/RCP} = (\mathbf{e}_s(\theta) \mp i\mathbf{e}_p(\theta))/\sqrt{2}$ , where  $\mathbf{e}_s(\theta)$  ( $\mathbf{e}_p(\theta)$ ) denote the direction of  $s$  ( $p$ ) polarization with the incidence angle  $\theta$ . As in our previous experiments<sup>49,50,59</sup>, we fix  $\theta = 65^\circ$  and  $\hbar\omega_{pr} = 21.7$  eV.

In Fig. 2c we present the circular dichroism  $I_{CD}(\mathbf{k}, E) = I_{LCP}(\mathbf{k}, E) - I_{RCP}(\mathbf{k}, E)$ , calculated from Eq. (4) (in absence of a pump pulse), where the polarization vector  $\mathbf{e}_{LCP/RCP}$  were inserted in the definition of the matrix elements Eq. (2). The circular dichroism in the angular distribution (CDAD) for binding energies close to the VBM is predominantly positive (negative) at K (K'), displaying its direct connection to the OAM. The structure of the CDAD is more complex around the top edge of the Brillouin zone, which is due to the specifics of the geometry, as  $\theta \neq 0$  breaks the reflection symmetry of the ARPES signal. Since for a 2D system  $L_z$  is the only relevant component, we would expect the one-to-one correspondence of the OAM only for normal incidence<sup>31</sup>. However, even for strongly tilted incidence angle ( $\theta = 65^\circ$ ) the CDAD provides an excellent qualitative map of the OAM texture. Therefore, the CDAD in the present geometry is

expected to be an excellent marker for the pump-induced modifications of the orbital texture.

**Floquet spectra.** Before presenting the CDAD in the presence of the driving pump pulse, we discuss the photodressed electronic structure and associated orbital texture. To this end we have calculated the retarded Green's function  $G_{\alpha\alpha}^R(\mathbf{k}, \omega)$ , including the interaction with the pump pulse via the Hamiltonian Eq. (3), and the Floquet spectral function

$$A(\mathbf{k}, \omega) = -\frac{1}{\pi} \text{Im} \sum_{\alpha} G_{\alpha\alpha}^R(\mathbf{k}, \omega), \quad (6)$$

which can be seen as a steady-state extension of the density of states. Eq. (6) is similar to the trARPES intensity Eq. (4) upon replacing the matrix elements  $M_{\alpha}(\mathbf{k}, E)M_{\alpha}^*(\mathbf{k}, E) \rightarrow \delta_{\alpha\alpha}$ .

We consider sub-gap (band gap in our model  $E_{\text{gap}} = 1.52$  eV) pumping  $\hbar\omega_p = 1.4$  eV for two reasons. (i) Red-detuned pumping is the most direct path to realizing the topologically non-trivial state in the conduction band manifold as discussed in ref. <sup>36</sup>. (ii) Absorption is strongly suppressed, which is crucial for avoiding laser-heating effects. While there would be pronounced resonant exciton features for the monolayer, the strong screening in the bulk sample reduces the exciton binding energy and oscillator strength. Hence, in this case, we neglect excitonic effects. The peak field strength of the pump pulse is chosen in the range  $E_0 = 1 \times 10^{-3}$  a.u. to  $E_0 = 2 \times 10^{-3}$  a.u., which corresponds to peak intensity  $I_0 \sim 3.5 \times 10^{10}$  W/cm<sup>2</sup> to  $I_0 \sim 1.4 \times 10^{11}$  W/cm<sup>2</sup>. This field strength range is well within the experimentally feasible regime.

Figure 3 shows the Floquet spectral function Eq. (6) for LCP pumps at two different field strength. For clarity of the discussion, we ignore spin-orbit coupling (SOC) at this point. The driven

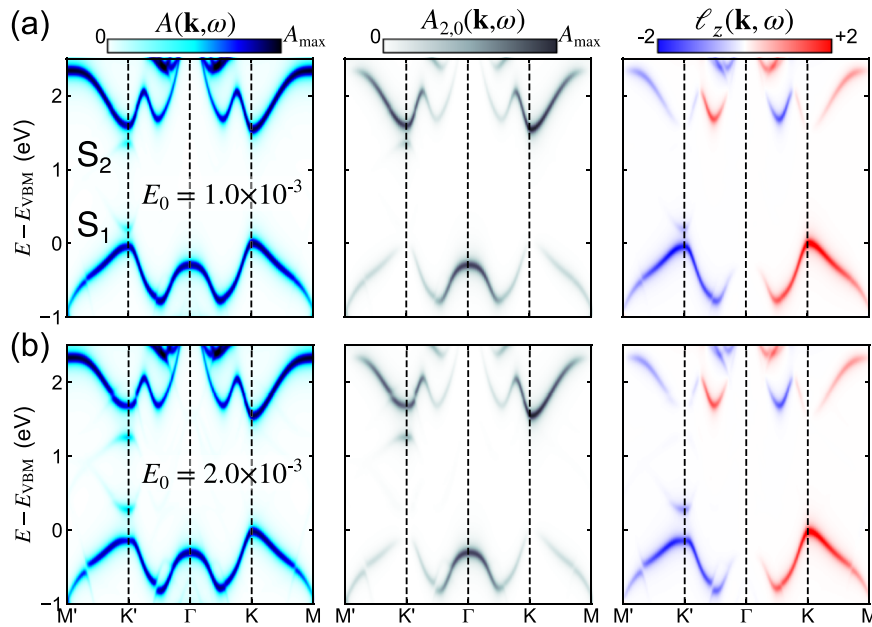


**Fig. 3 Floquet spectrum and orbital texture.** Spectral function  $A(\mathbf{k}, \omega)$  in the presence of a driving laser, associated spectral function  $A_{2,0}(\mathbf{k}, \omega)$  projected onto  $(\ell, m) = (2, 0) \equiv d_{z^2}$  orbitals, and orbital angular momentum texture  $\ell_z(\mathbf{k}, \omega)$  defined by Eq. (7), for (a)  $E_0 = 1.0 \times 10^{-3}$  a.u., and (b)  $E_0 = 2.0 \times 10^{-3}$  a.u. peak pump field strength. The pump photon energy is  $\hbar\omega_p = 1.4$  eV and the pump field is left-handed circularly polarized.

band structure exhibits only subtle changes in this regime, apart from small gap openings in the first conduction band and top valence band at  $K'$ . Note the optical absorption selection rules suppress photodressing at  $K$  points. The most striking features are the side-band features  $S_1$  ( $S_2$ ) directly above (below) the valence (conduction) band. These side bands separate further from the main bands upon increasing the pump strength, indicating light-induced orbital hybridization. To elucidate the orbital texture of these Floquet features, we have projected the Floquet spectral function Eq. (6) onto the Wannier functions  $|\varphi_{\mathbf{k}, \ell, m}\rangle$  in angular momentum basis. The projected spectral function  $A_{\ell, m}(\mathbf{k}, \omega)$  thus describes the energy- and momentum resolved orbital weight of  $|\varphi_{\mathbf{k}, \ell, m}\rangle$ . The Floquet spectrum for  $(\ell, m) = (2, 0) \equiv d_{z^2}$  orbital is dominant for the first conduction band at  $K/K'$  and for the side-band  $S_2$ .

The orbital-projected spectral function  $A_{\ell, m}(\mathbf{k}, \omega)$  also allows to define the spectral density of OAM via

$$\ell_z(\mathbf{k}, \omega) = \sum_{\ell, m} m A_{\ell, m}(\mathbf{k}, \omega). \quad (7)$$

Note that Eq. (7) is an approximation ignoring non-local contributions of self-rotating Bloch states<sup>60</sup>. Nevertheless, including the local orbital contributions only has been shown to be accurate for  $\text{WSe}_2$  in refs. 29,30. The OAM texture Eq. (7) is shown in the right panels in Fig. 3. At  $K/K'$  the OAM reflects the magnetic orbital character as sketched in Fig. 2a. Interestingly, the side-band  $S_1$  inherits the OAM texture of the top valence band.

The character of the involved orbitals and their hybridization can be further pinned down by projecting into the relevant subset of orbitals. This is achieved by the downfolding technique (we use the quadratic muffin-tin orbital method from ref. 61). We start from Floquet Hamiltonian

$$\mathcal{H}_{n, n'}(\mathbf{k}) = \frac{1}{T_p} \int_0^{T_p} dt e^{i(n-n')\omega_p t} H_{\alpha\alpha'}(\mathbf{k}, t) - n\omega_p \delta_{\alpha\alpha'} \delta_{nn'}, \quad (8)$$

where  $n, n'$  label the photon ladder. Diagonalizing the Floquet Hamiltonian Eq. (8) yields the photodressed bands; it is also used to compute the NESS Green's functions Eq. (5). To understand the

orbital texture of  $S_2$ , we downfold onto the subspace  $\{(d_{z^2}, n = 0), (d_{-2}, n = -1), (d_{+2}, n = +1)\}$  (see Fig. 4a for an illustration). This set corresponds to the original conduction band ( $d_{z^2}, n = 0$ ), the first side band of the top valence band upon absorbing one photon ( $d_{-2}, n = -1$ ), and the first side band of a higher-lying conduction band ( $d_{+2}, n = +1$ ) upon emitting photon. Downfolding the full Floquet Hamiltonian Eq. (8) into this subspace yields an effective  $3 \times 3$  Hamiltonian; the corresponding structure is shown (as dashed lines) in Fig. 4b, c. The excellent match of the first-principle Floquet spectrum and the downfolded bands underline that the orbital texture is captured by these few orbitals. While  $S_2$  originates from the  $d_{-2}$ -dominated valence band, the top of the side band acquires  $d_{z^2}$  character. The two other bands passing through the original conduction band exhibit orbital inversion stemming from the conduction band and the side-band of the higher-lying  $d_{+2}$  crossing. Consistent with ref. 36, these two bands—viewed as eigenstates of a static Hamiltonian—form a Chern insulator state with Chern number  $C = 1$ .

The orbital texture of  $S_1$  (Fig. 4a) is simpler: the photodressed top valence band retains its  $d_{-2}$  character, while the first side band of the conduction band (minus a photon) acquires some  $d_{-2}$  character in addition to its predominant  $d_{z^2}$  weight (Fig. 4d, e). This transfer of orbital weight is compensated by the gain of  $d_{z^2}$  character of  $S_2$ .

Although the Floquet-topological state is realized in the conduction band, the steady-state orbital weight—which determines the observable photoemission intensity—follows the original (trivial)  $d_{z^2}$  band. Hence, the total occupation-weighted Berry curvature is vanishingly small, since the Berry curvature of the upper and lower band are opposite. Evidencing the light-induced topological state by a quantized Hall response (which probes the global—momentum integrated—topological nature of the system) is thus not feasible. The orbital weight transfer in the side bands  $S_1$  and  $S_2$ , on the other hand, is a fingerprint of the topological state since the specific hybridizations and the resulting orbital textures are tied to the topological state. Therefore, one needs to have an observable which is sensitive to the local (in momentum-space) topological character of the band structure. As explained in the Introduction, this can be achieved by looking at

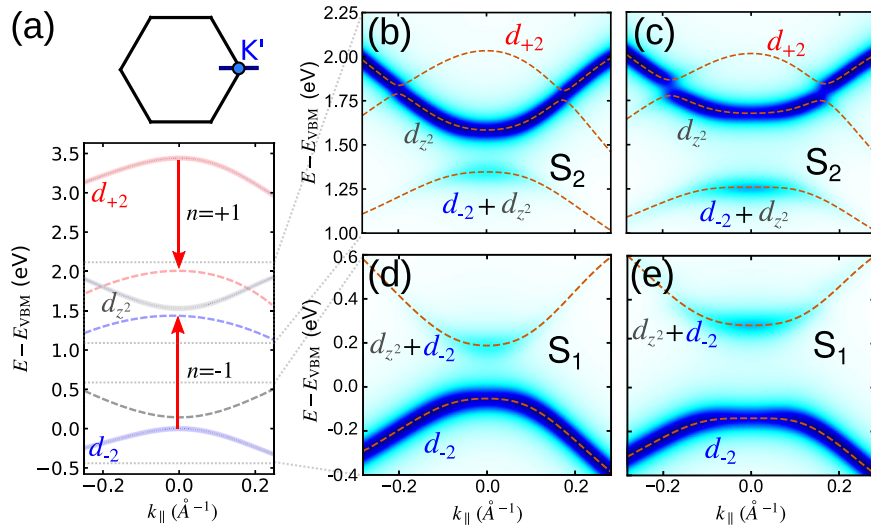


**Fig. 4 Orbital character of Floquet side bands.** **a** Sketch of the band structure and dominant orbitals near  $K'$  along the sketched path in reciprocal space. The dashed lines are periodic replicas of the bottom conduction band (gray), top valence band (blue), and a higher conduction band (red), respectively. **b** Zoom into the region close to the side-band features  $S_2$  in Fig. 3 for  $E_0 = 1 \times 10^{-3}$  a.u., and **c**  $E_0 = 2 \times 10^{-3}$  a.u. peak field strength. **d** Zoom into the region of  $S_1$  for  $E_0 = 1.0 \times 10^{-3}$  a.u., and **e**  $E_0 = 2 \times 10^{-3}$  a.u. pump amplitude. The dashed lines in **b-e** represent the band structure of the downfolded model.

the photoemission intensity modulation upon swapping the helicity of the ionizing probe pulse, i.e. by measuring the CDAD.

**Pump-probe circular dichroism.** Exploiting the helicity of the circularly polarized probe pulse, the orbital texture of the side bands can be accessed. In particular, we consider the CDAD as a direct probe of magnetic properties and orbital symmetry<sup>31</sup>. We compute the photoemission spectrum from Eq. (4) using the full matrix elements Eq. (2). At equilibrium, this approach reproduces the CDAD in Fig. 2b, while in the presence of the driving laser pulse, we can directly study the CDAD of the Floquet features and thus access its orbital texture.

We focus on the orbital texture of the side bands  $S_{1,2}$ . Figure 5 presents the pump-probe photoemission intensity and the CDAD (measured by swapping the ellicity of circularly polarized probe pulse), for the driven WSe<sub>2</sub> sample. Due to optical selection rules, for the sample orientation in Fig. 5a, the LCP pump gives rise to Floquet side bands only in the vicinity of the  $K'$  valleys, as in Fig. 3. Hence, the intensity (Fig. 5b, d) exhibits a threefold symmetric pattern, with pronounced features at the  $K'$  points. Inspecting the CDAD of  $S_1$  (Fig. 5c), we observe negative CDAD, while the CDAD of  $S_2$  shows, when averaged around the  $K'$  valleys, positive (negative) CDAD for  $k_x > 0$  ( $k_x < 0$ ).

Now we consider the sample rotated by 60° and pumped by RCP light (Fig. 5f). Since this sample rotation is equivalent to a time-reversal operation, also the pump polarization needs to be time-reversed for the side bands to appear at the same position (same valleys) in momentum space. While the intensity of  $S_1$  is very similar, the valley-averaged CDAD changes its sign. This behavior is a clear indication of the OAM reversing its sign, which is consistent with the acquired  $d_{-2}$  ( $d_{+2}$ ) character of the side band of the original conduction band. Indeed, if we assume that only the  $d_{\pm 2}$  orbital contributes to the matrix element Eq. (2), one finds for the corresponding CDAD  $I_{CD}^{(2,+2)}(\mathbf{k}, E) \approx -I_{CD}^{(2,-2)}(\mathbf{k}, E)$  on completely general grounds (Supplementary Note 2). This equality holds for normal incidence.

In contrast to the behavior of  $S_1$ , the CDAD of  $S_2$  does not show an overall sign reversal (except for some subtle intra-valley modifications). This is consistent with  $d_{22}$  orbital character, which is not affected by the time-reversal operation upon rotating by

60°. Furthermore, the sign change along  $k_x$  is indicative of  $d_{-2}$  character. As shown in the Supplementary Note 2, the CDAD for a Bloch state comprised of only the  $d_{22}$  orbital obeys  $I_{CD}^{(2,0)}(-k_x, k_y, E) = -I_{CD}^{(2,0)}(k_x, k_y, E)$ .

In summary, the CDAD of the side bands directly reflects the orbital character acquired by the hybridization of the valence band and a replica of the conduction band ( $S_1$ ) or the hybridization of the conduction band a copy of the valence band ( $S_2$ ).

**Robustness of dichroic markers against dissipation.** The CDAD of the Floquet side bands and their behavior under rotating the crystal (effective time-reversal operation) allows us to define dichroic markers, which are expected to be robust and thus measurable in experiments. In the present geometry, the CDAD for  $k_y \leq 0$  is less affected by extrinsic (geometric) matrix-element effects within the  $K'$  valleys; hence, we focus on the CDAD around  $K'_{1,2}$  as illustrated in Fig. 6a. We define the valley-integrated intensity  $I_{av}(K'_{1,2}, E)$  and CDAD  $I_{CD}(K'_{1,2}, E)$ , where the momentum integration is performed over the dashed squares in Fig. 6a. Because the same (opposite) sign of the CDAD around  $K'_{1,2}$  is expected for  $S_1$  ( $S_2$ ), we introduce the dichroic markers

$$A_1(E) = \frac{I_{CD}(K'_1, E)}{I_{av}(K'_1, E)} + \frac{I_{CD}(K'_2, E)}{I_{av}(K'_2, E)}, \quad (9)$$

$$A_2(E) = \frac{I_{CD}(K'_1, E)}{I_{av}(K'_1, E)} - \frac{I_{CD}(K'_2, E)}{I_{av}(K'_2, E)}. \quad (10)$$

Given the expected momentum dependence of the dichroism for  $d_{22}$  and  $d_{-2}/d_{+2}$  orbitals explained above, a peak in  $A_1(E)$  ( $A_2(E)$ ) would reflect a state with strong  $d_{-2}/d_{+2}$  ( $d_{22}$ ) character. These markers hence allow reducing complex momentum-resolved CDAD into integrated quantities that are directly reflecting the orbital character of a given equilibrium or light-induced state. The normalization to the intensity allows for a direct comparison under different pump and dissipation conditions. In Fig. 6b, c we present the marker Eq. (9) for both crystal orientations. The dichroic marker shows two distinct peaks that correspond to the states with pronounced OAM. The first peak originates from the top valence band with its almost unchanged  $d_{-2}$  character, while

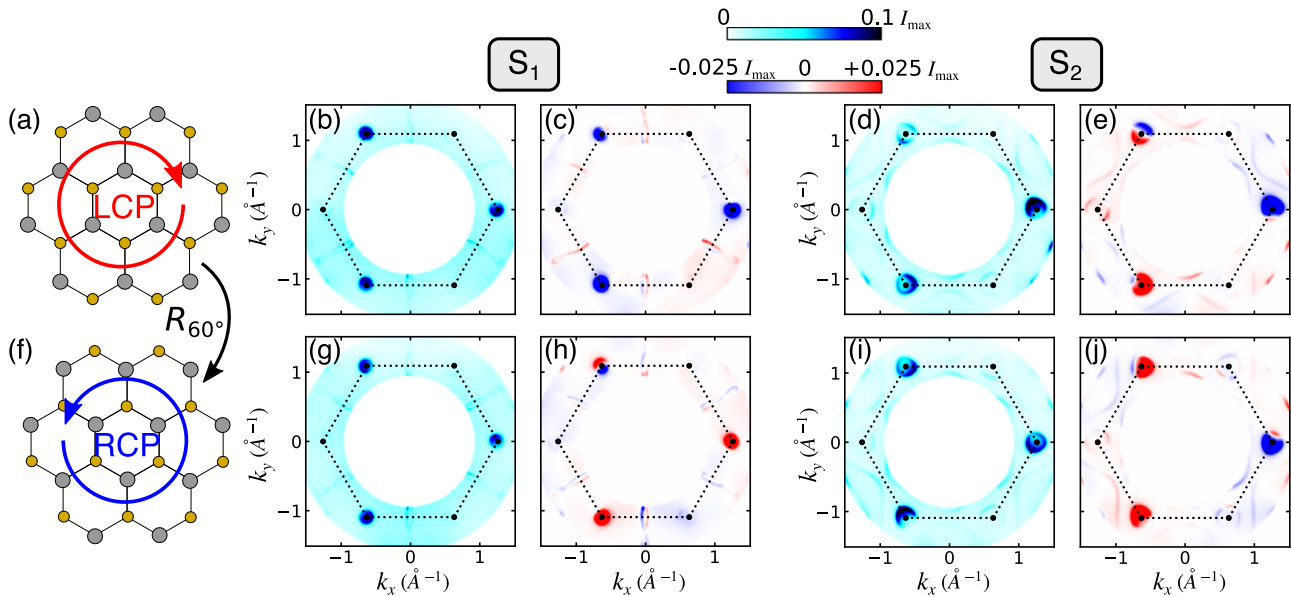


**Fig. 5 Intensity and circular dichroism of Floquet side bands.** **a** Sketch of the sample orientation and left-hand circular polarization (LCP) of the pump for the spectra in **b–e**. **b** Photoemission intensity at a fixed-energy cut through the side-band  $S_1$ ; **c** corresponding circular dichroism. **d, e** Analogous plots of intensity and circular dichroism for a fixed-energy cut through the side-band feature  $S_2$ . **f** Sketch of rotated sample and right-hand circular polarization (RCP) of the pump, which is the setup for the spectra in **g–j**. The intensity for  $S_1/S_2$  is shown in **g, i**, while the circular dichroism is presented in **h, j**. The binding energy  $E$  is chosen to maximize the intensity; the pump field strength is  $E_0 = 2 \times 10^{-3}$  a.u., corresponding to Fig. 3b.

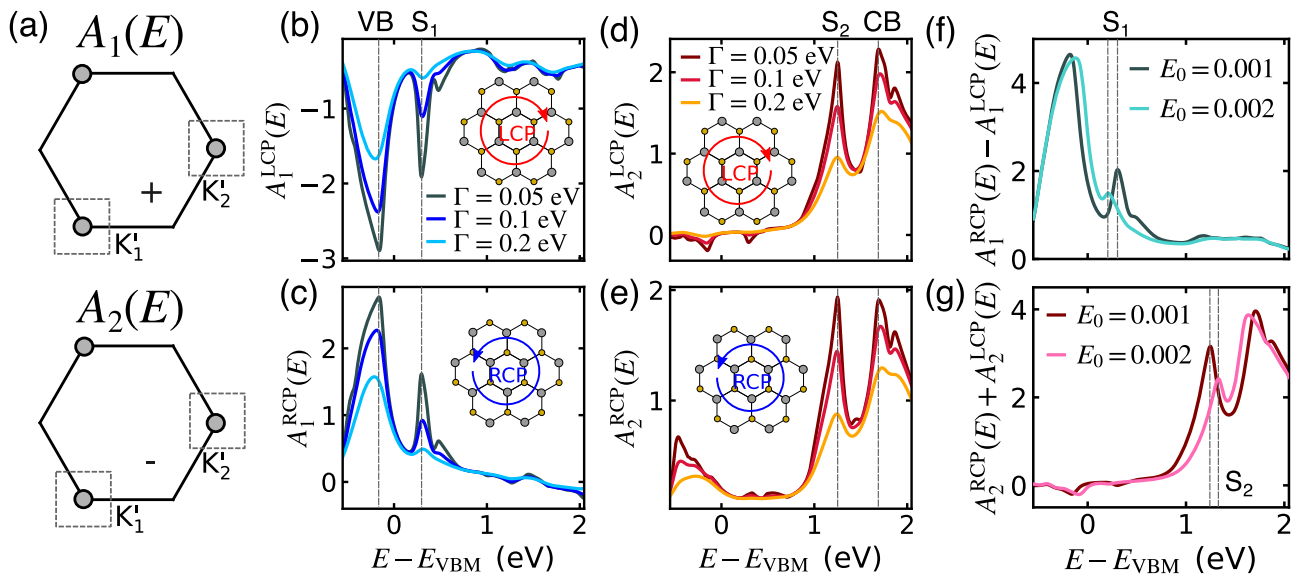


**Fig. 6 Dichroic markers and robustness against dissipation.** **a** Illustration of the definition of the dichroic markers  $A_{1,2}(E)$  for the side bands  $S_{1,2}$ . **b** dichroic marker  $A_1(E)$  for the orientation and left-hand circularly polarized pump as in Fig. 5a, and **c** for orientation and right-hand circularly polarized pump as in Fig. 5f. **d, e** dichroic marker  $A_2(E)$  for crystal orientation as in **b, c**. The pump field strength is  $E_0 = 2 \times 10^{-3}$  a.u. in **b–e**, and the signal for different bath coupling strength  $\Gamma$  is shown. We also indicate the position of the valence band (VB), side band band ( $S_{1,2}$ ), and conduction band (CB) peaks. **f** Time-reversal difference of the marker  $A_1(E)$  for  $\Gamma = 0.1$  eV for different field strength of the pump. The dashed lines in **b, c, f** indicate the position of the side band  $S_1$ , while they indicate  $S_2$  in **d, e, g**.

the second peak reflects the acquired  $d_{-2}$  character of  $S_1$  (Fig. 3). This peak is very pronounced for low to moderate dissipation and remains visible even for a bath coupling strength of  $\Gamma = 0.2$  eV. The corresponding energy smearing ( $\sim 80$  meV) is larger than the spectral resolution that can be achieved in trARPES setups<sup>37,40</sup>. Note that the sign of peaks changes upon applying the time-reversal operation, which reverses the OAM of the magnetic orbitals  $d_{-2} \leftrightarrow d_{+2}$ .

Inspecting the marker Eq. (10) sensitive to sign changes along  $k_x$ , we see that most of the features near the VBM cancel, while the region close to the conduction band is highlighted. There is a pronounced peak corresponding to  $S_2$  and to the lowest conduction band. Both peaks are attributed to  $d_{-2}$  orbital character. The  $S_2$  peak is even more robust against dissipation than the  $S_1$  peak.

The sign reversal of the marker Eq. (9) and absence thereof in the marker Eq. (10) upon crystal rotation prompts us to symmetrize or

anti-symmetrize, respectively, the energy-resolved dichroic markers. To highlight the reversal of the OAM, we calculated the difference of the dichroic marker Eq. (9) upon effective time-reversal operation, shown in Fig. 6f. Similarly, the calculated average upon effective time-reversal operation highlights the nonmagnetic orbitals and  $d_{z^2}$  in particular (Fig. 6g). As Fig. 6f, g demonstrate, for moderate strength of the dissipation  $\Gamma = 0.1$  eV the  $S_{1,2}$  peaks remain visible even an amplitude of the pump pulse as weak as  $E_0 = 10^{-3}$  a.u.

Note that we have excluded spin-orbit coupling (SOC) in the results presented here for clarity of the discussion. Neglecting the SOC is justified by the pronounced spin splitting of the top valence band. In the sub-gap pumping regime, the split-off Floquet side band is clearly separated from the conduction band and thus far off-resonant. The hybridization of the Floquet side bands and the valence and conduction band is suppressed, and the photoemission intensity of the side bands is about two orders of magnitude lower. Hence, our simulations without SOC are predictive. This is underpinned by additional calculations including SOC in the Supplementary Note 3.

**Effects of laser-assisted photoemission.** Replica of the original bands in the trARPES signal can also occur due to LAPE<sup>11</sup>, which describes transitions from the occupied bands to the Floquet-Volkov ladder of periodic replica of photoelectron states. Thus, LAPE typically gives rise to photoemission intensity overlapping (and also interfering<sup>62</sup>) with Floquet side bands. To investigate the robustness of the dichroic features in more realistic conditions, we extended the theory of trARPES by including the Floquet-Volkov ladder. In combination with the Floquet NESS formalism, we obtain a straightforward generalization of Eq. (4) that captures both Floquet and LAPE effects (see methods section). Equipped with this powerful approach we computed the trARPES signals and extracted the dichroic markers in an analogous fashion as above.

In Fig. 7a we compare the trARPES intensity without LAPE (left-hand side) to the case with LAPE fully included. As expected, LAPE enhances the intensity of the side band structures throughout the Brillouin zone; the optical selection rules that govern the orbital hybridization and the photodressing of the bands do not apply for LAPE. At  $K'$ , the intensity of the side band features  $S_{1,2}$  is almost unaffected by LAPE. In particular, as LAPE results in exact replica of the valence band (as seen at  $K$ ), while the feature  $S_2$  is pushed to lower energies, strongly suppresses interference effects.

Inspecting the dichroic markers upon including LAPE (Fig. 7b, c) reveals that the characteristic peaks remain qualitatively unaffected. In particular, for  $S_1$  the spectral weight associated to LAPE is negligible (Fig. 7b), while the dichroic marker highlighting  $S_2$  (Fig. 7c) shows a slight reduction of the  $S_2$  peak. The only qualitatively different features due to LAPE is a peak slightly below the energy of  $S_2$  in Fig. 7b. As the definition of the marker  $A_1(E)$  (Eq. 9) highlights the signal originating from the magnetic orbitals  $d_{\pm 2}$ , a direct replica of the valence band due to LAPE manifest as a peak in  $A_1(E)$  in the energy region below the conduction band.

## Discussion

In summary, we presented how the local topological properties and orbital texture of pumped  $2H\text{-WSe}_2$  manifest in circular dichroism in time-resolved ARPES. Combining first-principle light-matter coupling and a highly accurate model for the photoemission matrix elements allowed us to predict the distinct dichroic features under realistic experimental conditions. In this setup, the manifestation of the topological state is masked by the quasi-thermal population of the Floquet bands. However, the

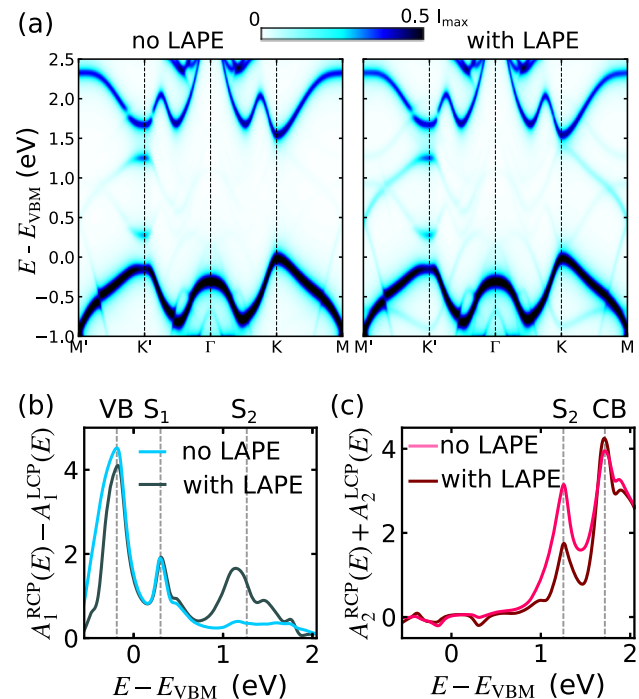


**Fig. 7** Effects of LAPE on spectra and dichroic markers. **a** Comparison of the unpolarized trARPES signal  $I_{av}(\mathbf{k}, E)$  without (left panel) and with (right panel) including laser-assisted photoemission (LAPE), for a left-hand circularly polarized (LCP) pump and the crystal orientation as in Fig. 6a. **b, c** Time-reversal difference of the dichroic markers as in Fig. 6f, g including LAPE (RCP: right-hand circularly polarized). The pump strength is  $E_0 = 2 \times 10^{-3}$  a.u. and the bath coupling is set to  $\Gamma = 0.1$  eV in all plots.

orbital texture of the side bands—which is intimately connected to the induced topology—gives rise to distinct CDAD. Defining robust observables that are sensitive to the orbital character, we showed that we can access the light-induced orbital texture, even for strong dissipation and relatively weak pump fields. Focusing on the CDAD as a hallmark of the Floquet state also allows to disentangle LAPE contributions from photodressing effects. The dichroic markers in the relevant energy region are qualitatively unaffected as LAPE contributions to the dichroism effectively cancel out.

Therefore—supported by our predictive calculations—measuring the pump-probe CDAD is an ideal platform to evidence the emergence of light-induced topological state in  $2H\text{-WSe}_2$  in forthcoming experiments. Indeed, while time-resolved CD-ARPES in the XUV spectral range (allowing extending the photoemission horizon up to Brillouin zone edges (e.g.  $K/K'$ )) has never been archived yet, all the technological building blocks allowing to performed these experiments have been demonstrated independently and are currently being put together by some experimental groups<sup>63</sup>. The last step towards time-resolved CD-ARPES in the XUV spectral range is to achieved polarization control of high-repetition-rate XUV source, which is not fundamentally different to what has been already demonstrated for femtosecond XUV source pumped by Ti:Sa drivers, operating at moderate repetition rate<sup>46,64</sup>. This is allowing us to believe that the methodology described in this manuscript is experimentally within reach.

In addition, recent static CDAD ARPES experiments also showed the signatures of Berry curvature from Weyl semimetals<sup>32</sup>, time-resolved CDAD ARPES would thus also be a powerful tool to evidence Floquet-Weyl states<sup>65</sup> and other light-induced topological phenomena.

## Methods

**Wannier functions and photoemission matrix elements.** We computed the electronic structure of monolayer WSe<sub>2</sub> using the QUANTUM ESPRESSO package<sup>66</sup>. We used the PBE functional and norm-conserving pseudopotentials from the PSEUDODOJO project<sup>67</sup>. We constructed symmetry-adapted maximally localized Wannier functions to retain the *d* and *p* orbital character associated to the W and Se sites, respectively. More details on the calculations and extracting the velocity matrix elements  $\mathbf{v}_{\alpha\alpha'}(\mathbf{k})$  can be found in ref. <sup>55</sup>.

The atomic photoemission matrix elements Eq. (2) are computed from the Wannier functions  $\phi_j(\mathbf{r})$ . We approximate the real-space dependence by

$$\phi_j(\mathbf{r}) = R_j(r)X_{\ell_j m_j}(\hat{\mathbf{r}}), \quad (11)$$

where  $X_{\ell m}(\hat{\mathbf{r}})$  denotes the real spherical harmonics. We assume that all *d* (*p*) orbitals possess the same radial dependence:  $R_j(r) = R_d(r)$  ( $R_j(r) = R_p(r)$ ).

Following ref. <sup>50</sup>, we compute the photoemission matrix elements by (i) switching to length gauge by replacing  $\hat{\mathbf{p}} = -i\hat{H}, \hat{\mathbf{r}}$ , where  $\hat{\mathbf{r}}$  is the dipole operator, and (ii) approximating the final states by plane waves. We obtain

$$M_{\alpha}(\mathbf{k}, E) = -i(E - \varepsilon_{\alpha}(\mathbf{k})) \sum_j C_{j\alpha}(\mathbf{k}) e^{i\gamma_j} e^{-i\mathbf{p}\cdot\mathbf{t}_j} \times \int d\mathbf{r} e^{-i\mathbf{p}\cdot\mathbf{r}} \mathbf{e} \cdot \mathbf{r} R_j(r) X_{\ell_j m_j}(\hat{\mathbf{r}}), \quad (12)$$

where  $\mathbf{p}$  is the three-dimensional photoelectron momentum vector defined by  $\mathbf{p}_{\parallel} = \mathbf{k}$  and  $\mathbf{p}^2/2 = E + V_0$  ( $V_0$  is the inner potential), and where  $\mathbf{t}_j$  denote the positions of the W and Se atoms in the unit cell. The probe polarization is denoted by the complex unit vector  $\mathbf{e}$ . The integral in Eq. (12) is evaluated by expanding the plane waves in real spherical harmonics. This leads to two radial integrals

$$I_j^{\pm}(E) = \int_0^{\infty} dr r^3 j_{\ell_j \pm 1}(\sqrt{2Er}) R_j(r), \quad (13)$$

where  $j_{\ell}(x)$  denotes the spherical Bessel functions. The energy dependence of the radial integrals  $I_j^{\pm}(E)$  is weak in the XUV regime, therefore we  $\sim I_j^{\pm}(E) \approx I_j^{\pm}$ , which correspond to four ( $j = d, p$ ) independent parameters. Together with the inner potential  $V_0$  and the 11 phase factors  $\gamma_j$ , there are 17 free parameters. We determined these parameters such that the resulting photoemission intensity  $I(\mathbf{k}, E)$  for *s* and *p* polarized at binding energy  $E - E_{\text{VBM}} = -0.2$  eV fits the experimental signals (see Supplementary Note 1 for a direct comparison).

**Floquet NESS formalism.** We assume that each lattice site (independent of the orbital) is coupled to a thermalizing bath within the wide-band limit approximation (WBLA). The effects of the bath on the system is captured by the self-energy, which is then used to calculate the Green's function. It is convenient to express these quantities in the basis of the Floquet Hamiltonian Eq. (8). In this basis, the retarded part of the self-energy reads

$$\Sigma_{\alpha n, \alpha' n'}^{\text{R}}(\omega) = -i \frac{\Gamma}{2} \delta_{\alpha\alpha'} \delta_{nn'} \delta_{nn'}, \quad (14)$$

while the lesser part (which determines the occupation of the Floquet bands) is given by

$$\Sigma_{\alpha n, \alpha' n'}^{\text{<}}(\mathbf{k}, \omega) = i\Gamma \delta_{\alpha\alpha'} \delta_{nn'} n_{\text{F}}(\omega - \mu + n\omega_{\text{p}}). \quad (15)$$

Here,  $n_{\text{F}}(\omega)$  denotes the Fermi function, which also includes the effective temperature  $T_{\text{eff}}$ . Representing the self-energies Eq. (14)–(15) by compact matrices in band-Floquet space, the Floquet Green's function is then determined solving the Dyson equation

$$[\hat{\mathcal{G}}^{\text{R}}(\mathbf{k}, \omega)]^{-1} = \omega - \hat{H}(\mathbf{k}) - \hat{\Sigma}^{\text{R}}(\mathbf{k}, \omega) \quad (16)$$

and the Keldysh equation

$$\hat{\mathcal{G}}^{\text{<}}(\mathbf{k}, \omega) = \hat{\mathcal{G}}^{\text{R}}(\mathbf{k}, \omega) \hat{\Sigma}^{\text{<}}(\omega) [\hat{\mathcal{G}}^{\text{R}}(\mathbf{k}, \omega)]^{\dagger}. \quad (17)$$

Once the Floquet Green's functions have been computed from Eqs. (17)–(17), the physical Green's functions entering the spectra can be obtained, as explained below.

**Time-resolved photoemission and laser-assisted processes.** The Floquet NESS formalism also allows to compute the trARPES signal in the limit of long pump and probe pulses. We start from the general expression for trARPES<sup>56</sup>,

$$I(\mathbf{p}, \Delta t) = \text{Im} \sum_{\alpha\alpha'} M_{\alpha}^*(\mathbf{p}) M_{\alpha'}(\mathbf{p}) \int_0^{\infty} dt \int_0^t dt' s(t) s(t') \times G_{\alpha\alpha'}^{\text{<}}(\mathbf{k}; t', t) e^{i\Phi(\mathbf{p}; t, t')}, \quad (18)$$

where  $s(t)$  denotes the envelop of the probe pulse, and

$$\Phi(\mathbf{p}; t, t') = \frac{1}{2} \int_{t'}^t d\bar{t} (\mathbf{p} - q\mathbf{A}(\bar{t}))^2 \quad (19)$$

accounts for the laser-dressed final (Volkov) states. For brevity we introduced the three-dimensional photoelectron momentum  $\mathbf{p}$  as in Eq. (12). The time-dependent Green's function entering Eq. (18) can be expressed in terms of the Floquet Green's

function Eq. (17):

$$G_{\alpha\alpha'}^{\text{<}}(\mathbf{k}; t, t') = \sum_{nn'} \int_{-\omega_{\text{p}}/2}^{\omega_{\text{p}}/2} \frac{d\omega}{2\pi} G_{\alpha n, \alpha' n'}^{\text{<}}(\mathbf{k}, \omega) e^{-i\omega(t-t')} \times e^{-in\omega_{\text{p}}t} e^{-in'\omega_{\text{p}}t'}. \quad (20)$$

Now we take the limit of long pulses  $s(t) \rightarrow 1$ ; in this limit it is convenient to switch to average and relative time representation  $t_{\text{av}} = (t + t')/2$ ,  $t_{\text{rel}} = t - t'$ . If LAPE effects can be neglected, the phase Eq. (19) simplifies to  $\Phi(\mathbf{p}; t, t') = Et_{\text{rel}}$ , and the trARPES expression Eq. (18) reduces to Eq. (4) with the effective frequency-space Green's function

$$G_{\alpha\alpha'}^{\text{R, <}}(\mathbf{k}, \omega) = \sum_n G_{\alpha n, \alpha' n}^{\text{R, <}}(\mathbf{k}, \omega - n\omega_{\text{p}}) \Lambda(\omega - n\omega_{\text{p}}), \quad (21)$$

where  $\Lambda(\omega) = 1$  if  $-\omega_{\text{p}}/2 < \omega < \omega_{\text{p}}/2$  and zero otherwise.

To capture for LAPE effects the time-dependent phase Eq. (19) needs to be included explicitly. Inserting the two-time representation Eq. (20) into Eq. (18) and expanding Eq. (19) in a Fourier series with respect to  $t_{\text{av}}$ , we recover a similar expression as Eq. (4):

$$I(\mathbf{k}, E) \propto \text{Im} \sum_{\alpha\alpha'} M_{\alpha}(\mathbf{k}, E) \tilde{G}_{\alpha\alpha'}^{\text{<}}(\omega_{\text{pr}} - E) M_{\alpha'}^*(\mathbf{k}, E). \quad (22)$$

Here, we have introduced the LAPE-augmented effective Green's function

$$\tilde{G}_{\alpha\alpha'}^{\text{<}}(\omega) = \sum_l \sum_{nn'} G_{\alpha n, \alpha' n'}^{\text{R, <}} \left( \mathbf{k}, \omega - \frac{n + n' + l}{2} \omega_{\text{p}} \right) \times \Lambda \left( \omega - \frac{n + n' + l}{2} \omega_{\text{p}} \right) L_l^{n' - n}(\omega) \quad (23)$$

with the LAPE kernel

$$L_l^m(\omega) = \frac{e^{-im\theta}}{2T_{\text{p}}} \int_0^{2T_{\text{p}}} dt e^{i\omega t/2} J_m \left( x_0 \sin \frac{\omega_{\text{p}} t}{2} \right). \quad (24)$$

Here,  $T_{\text{p}} = 2\pi/\omega_{\text{p}}$ ,  $x_0 = qE_0 |\mathbf{e} \cdot \mathbf{p}| / \omega_{\text{p}}^2$ , and  $\theta = \arg(\mathbf{e} \cdot \mathbf{p})$ .

## Data availability

The referenced experimental data and the Wannier model are available at the repository [schuel\\_m/fitting-matrix-elements](https://gitlab.psi.ch/schuel_m/fitting-matrix-elements) at [gitlab.psi.ch](https://gitlab.psi.ch).

## Code availability

The script performing the fitting procedure are available at the repository [schuel\\_m/fitting-matrix-elements](https://gitlab.psi.ch/schuel_m/fitting-matrix-elements) at [gitlab.psi.ch](https://gitlab.psi.ch). The custom computer codes used obtain the results are available upon reasonable request.

Received: 25 January 2022; Accepted: 13 June 2022;

Published online: 27 June 2022

## References

- Basov, D. N., Averitt, R. D. & Hsieh, D. Towards properties on demand in quantum materials. *Nat. Mater.* **16**, 1077–1088 (2017).
- de la Torre, A. et al. Colloquium: Nonthermal pathways to ultrafast control in quantum materials. *Rev. Mod. Phys.* **93**, 041002 (2021).
- Oka, T. & Aoki, H. Photovoltaic Hall effect in graphene. *Phys. Rev. B* **79**, 081406 (2009).
- Wang, Y. H., Steinberg, H., Jarillo-Herrero, P. & Gedik, N. Observation of floquet-bloch states on the surface of a topological insulator. *Science* **342**, 453–457 (2013).
- Mahmood, F. et al. Selective scattering between Floquet-Bloch and Volkov states in a topological insulator. *Nat. Phys.* **12**, 306–310 (2016).
- Sato, S. A. et al. Floquet states in dissipative open quantum systems. *J. Phys. B: At. Mol. Opt. Phys.* **53**, 225601 (2020).
- Sato, S. A. et al. Microscopic theory for the light-induced anomalous Hall effect in graphene. *Phys. Rev. B* **99**, 214302 (2019).
- Schüler, M. et al. How circular dichroism in time- and angle-resolved photoemission can be used to spectroscopically detect transient topological states in graphene. *Phys. Rev. X* **10**, 041013 (2020).
- Gierz, I. et al. Tracking primary thermalization events in graphene with photoemission at extreme time scales. *Phys. Rev. Lett.* **115**, 086803 (2015).
- Aeschlimann, S. et al. Survival of Floquet-Bloch states in the presence of scattering. *Nano Lett.* **21**, 5028–5035 (2021).
- Miñaja-Avila, L. et al. Laser-assisted photoelectric effect from surfaces. *Phys. Rev. Lett.* **97**, 113604 (2006).

12. Keunecke, M. et al. Electromagnetic dressing of the electron energy spectrum of Au(111) at high momenta. *Phys. Rev. B* **102**, 161403 (2020).
13. Broers, L. & Mathey, L. Detecting light-induced Floquet band gaps of graphene via trARPES. *arXiv* <http://arxiv.org/abs/2108.05351> (2021).
14. McIver, J. W. et al. Light-induced anomalous Hall effect in graphene. *Nat. Phys.* **16**, 38–41 (2020).
15. Broers, L. & Mathey, L. Observing light-induced Floquet band gaps in the longitudinal conductivity of graphene. *Commun. Phys.* **4**, 1–7 (2021).
16. Smallwood, C. L., Kaindl, R. A. & Lanzara, A. Ultrafast angle-resolved photoemission spectroscopy of quantum materials. *EPL* **115**, 27001 (2016).
17. Rohde, G. et al. Time-resolved ARPES with sub-15 fs temporal and near Fourier-limited spectral resolution. *Rev. Sci. Instrum.* **87**, 103102 (2016).
18. Lee, C. et al. High resolution time- and angle-resolved photoemission spectroscopy with 11 eV laser pulses. *Rev. Sci. Instrum.* **91**, 043102 (2020).
19. Maklar, J. et al. A quantitative comparison of time-of-flight momentum microscopes and hemispherical analyzers for time- and angle-resolved photoemission spectroscopy experiments. *Rev. Sci. Instrum.* **91**, 123112 (2020).
20. Moser, S. An experimentalist's guide to the matrix element in angle resolved photoemission. *J. Electron Spectrosc. Relat. Phenomena* **214**, 29–52 (2017).
21. Moser, S. The Huygens principle of angle-resolved photoemission. *arXiv* <http://arxiv.org/abs/2201.04576> (2022).
22. Liu, Y., Bian, G., Miller, T. & Chiang, T.-C. Visualizing electronic chirality and berry phases in graphene systems using photoemission with circularly polarized light. *Phys. Rev. Lett.* **107**, 166803 (2011).
23. Gierz, I., Lindroos, M., Höchst, H., Ast, C. R. & Kern, K. Graphene sublattice symmetry and isospin determined by circular dichroism in angle-resolved photoemission spectroscopy. *Nano Lett.* **12**, 3900–3904 (2012).
24. Wang, Y. H. et al. Observation of a Warped Helical spin texture in Bi<sub>2</sub>Se<sub>3</sub> from circular dichroism angle-resolved photoemission spectroscopy. *Phys. Rev. Lett.* **107**, 207602 (2011).
25. Lin, Chiu-Yun et al. Orbital-dependent spin textures in Bi<sub>2</sub>Se<sub>3</sub> quantum well states. *Phys. Rev. B* **98**, 075149 (2018).
26. Jozwiak, C. et al. Spin-polarized surface resonances accompanying topological surface state formation. *Nat. Commun.* **7**, 13143 (2016).
27. Fedchenko, O. et al. 4D texture of circular dichroism in soft-x-ray photoemission from tungsten. *New J. Phys.* **21**, 013017 (2019).
28. Razzoli, E. et al. Selective probing of hidden spin-polarized states in inversion-symmetric bulk MoS<sub>2</sub>. *Phys. Rev. Lett.* **118**, 086402 (2017).
29. Cho, S. et al. Experimental observation of hidden berry curvature in inversion-symmetric Bulk 2H-WSe<sub>2</sub>. *Phys. Rev. Lett.* **121**, 186401 (2018).
30. Cho, S. et al. Studying local Berry curvature in 2H-WSe<sub>2</sub> by circular dichroism photoemission utilizing crystal mirror plane. *Sci. Rep.* **11**, 1684 (2021).
31. Schüller, M. et al. Local Berry curvature signatures in dichroic angle-resolved photoelectron spectroscopy from two-dimensional materials. *Sci. Adv.* **6**, eaay2730 (2020).
32. Ünzelmann, M. et al. Momentum-space signatures of Berry flux monopoles in the Weyl semimetal TaAs. *Nat. Commun.* **12**, 3650 (2021).
33. Xiao, D., Chang, Ming-Che & Niu, Q. Berry phase effects on electronic properties. *Rev. Mod. Phys.* **82**, 1959–2007 (2010).
34. De Giovannini, U., Hübener, H. & Rubio, A. Monitoring electron-photon dressing in WSe<sub>2</sub>. *Nano Lett.* **16**, 7993–7998 (2016).
35. Liu, Ro-Ya et al. Femtosecond to picosecond transient effects in WSe<sub>2</sub> observed by pump-probe angle-resolved photoemission spectroscopy. *Sci. Rep.* **7**, 15981 (2017).
36. Claassen, M., Jia, C., Moritz, B. & Devereaux, T. P. All-optical materials design of chiral edge modes in transition-metal dichalcogenides. *Nat. Commun.* **7**, 13074 (2016).
37. Sie, E. J., Rohwer, T., Lee, C. & Gedik, N. Time-resolved XUV ARPES with tunable 24–33 eV laser pulses at 30 meV resolution. *Nat. Commun.* **10**, 3535 (2019).
38. Corder, C. et al. Ultrafast extreme ultraviolet photoemission without space charge. *Struct. Dyn.* **5**, 054301 (2018).
39. Buss, J. H. et al. A setup for extreme-ultraviolet ultrafast angle-resolved photoelectron spectroscopy at 50-kHz repetition rate. *Rev. Sci. Instrum.* **90**, 023105 (2019).
40. Cucini, R. et al. Coherent narrowband light source for ultrafast photoelectron spectroscopy in the 17–31 eV photon energy range. *Struct. Dyn.* **7**, 014303 (2020).
41. Mills, A. K. et al. Cavity-enhanced high harmonic generation for extreme ultraviolet time- and angle-resolved photoemission spectroscopy. *Revi. Sci. Instrum.* **90**, 083001 (2019).
42. Puppini, M. et al. Time- and angle-resolved photoemission spectroscopy of solids in the extreme ultraviolet at 500 kHz repetition rate. *Rev. Sci. Instrum.* **90**, 023104 (2019).
43. Chiang, Cheng-Tien et al. Boosting laboratory photoelectron spectroscopy by megahertz high-order harmonics. *New J. Phys.* **17**, 013035 (2015).
44. Keunecke, M. et al. Time-resolved momentum microscopy with a 1 MHz high-harmonic extreme ultraviolet beamline. *Rev. Sci. Instrum.* **91**, 063905 (2020).
45. Dohring, T., Schonhense, G. & Heinzmann, U. A circular polarizer for the region of windowless VUV radiation. *Meas. Sci. Technol.* **3**, 91–97 (1992).
46. Vodungbo, B. et al. Polarization control of high order harmonics in the EUV photon energy range. *Opt. Express* **19**, 4346–4356 (2011).
47. Yao, K. et al. A tabletop setup for ultrafast helicity-dependent and element-specific absorption spectroscopy and scattering in the extreme ultraviolet spectral range. *Rev. Sci. Instrum.* **91**, 093001 (2020).
48. von Korff Schmising, C. et al. Generating circularly polarized radiation in the extreme ultraviolet spectral range at the free-electron laser FLASH. *Rev. Sci. Instrum.* **88**, 053903 (2017).
49. Beaulieu, S. et al. Revealing hidden orbital Pseudospin texture with time-reversal dichroism in photoelectron angular distributions. *Phys. Rev. Lett.* **125**, 216404 (2020).
50. Schüller, M. et al. Polarization-modulated angle-resolved photoemission spectroscopy: toward circular dichroism without circular photons and Bloch wave-function reconstruction. *Phys. Rev. X* **12**, 011019 (2022).
51. Madéo, J. et al. Directly visualizing the momentum-forbidden dark excitons and their dynamics in atomically thin semiconductors. *Science* **370**, 1199–1204 (2020).
52. Beaulieu, S. et al. Ultrafast dynamical Lifshitz transition. *Sci. Adv.* **7**, eabd9275 (2021).
53. Dong, S. et al. Direct measurement of key exciton properties: energy, dynamics, and spatial distribution of the wave function. *Natural Sciences* **1**, e10010 (2021).
54. Rostami, H. et al. Layer and orbital interference effects in photoemission from transition metal dichalcogenides. *Phys. Rev. B* **100**, 235423 (2019).
55. Schüller, M., Marks, J. A., Murakami, Y., Jia, C. & Devereaux, T. P. Gauge invariance of light-matter interactions in first-principle tight-binding models. *Phys. Rev. B* **103**, 155409 (2021).
56. Schüller, M. & Sentef, M. A. Theory of subcycle time-resolved photoemission: application to terahertz photodressing in graphene. *J. Electron Spectrosc. Relat. Phenom.* **253**, 147121 (2021).
57. Murakami, Y., Tsuji, N., Eckstein, M. & Werner, P. Nonequilibrium steady states and transient dynamics of conventional superconductors under phonon driving. *Phys. Rev. B* **96**, 045125 (2017).
58. Freericks, J., Krishnamurthy, H. & Pruschke, T. Theoretical description of time-resolved photoemission spectroscopy: application to pump-probe experiments. *Phys. Rev. Lett.* **102**, 136401 (2009).
59. Beaulieu, S. et al. Unveiling the orbital texture of 1T-TiTe<sub>2</sub> using intrinsic linear dichroism in multidimensional photoemission spectroscopy. *npj Quantum Mater.* **6**, 1–11 (2021).
60. Caruso, F., Schebek, M., Pan, Y., Vona, C. & Draxl, C. Chirality of valley excitons in monolayer transition-metal dichalcogenides. *arXiv* <https://doi.org/10.48550/arXiv.2112.04781> (2021).
61. Zurek, E., Jepsen, O. & Andersen, OleKrogh Muffin-Tin orbital Wannier-like functions for insulators and metals. *ChemPhysChem* **6**, 1934–1942 (2005).
62. Park, SangTae Interference in Floquet-Volkov transitions. *Phys. Rev. A* **90**, 013420 (2014).
63. Comby, A. et al. Ultrafast polarization-tunable monochromatic extreme ultraviolet source at high-repetition-rate. *arXiv* <https://arxiv.org/abs/2205.04705> (2022).
64. Willems, F. et al. Probing ultrafast spin dynamics with high-harmonic magnetic circular dichroism spectroscopy. *Phys. Rev. B* **92**, 220405 (2015).
65. Hübener, H., Sentef, M. A., Giovannini, UmbertoDe, Kemper, A. F. & Rubio, A. Creating stable Floquet-Weyl semimetals by laser-driving of 3D Dirac materials. *Nat. Commun.* **8**, 1–8 (2017).
66. Giannozzi, P. et al. Quantum Espresso: a modular and open-source software project for quantum simulations of materials. *J. Phys.: Condens. Matter* **21**, 395502 (2009).
67. van Setten, M. J. et al. The PseudoDojo: training and grading a 85 element optimized norm-conserving pseudopotential table. *Comp. Phys. Commun.* **226**, 39–54 (2018).

### Acknowledgements

The calculations have been performed at the Merlin6 cluster at the Paul Scherrer Institute. M.S. thanks the Swiss National Science Foundation SNF for its support with an Ambizione grant (project No. 193527). S.B. acknowledge funding from Université de Bordeaux, CNRS and Quantum Matter Bordeaux.

### Author contributions

M.S. and S.B. conceived the project idea. M.S. performed all calculations and wrote the first draft. S.B. provided the experimental data in the supplementary material. Both authors worked on the manuscript together.

**Competing interests**

The authors declare no competing interests.

**Additional information**

**Supplementary information** The online version contains supplementary material available at <https://doi.org/10.1038/s42005-022-00944-w>.

**Correspondence** and requests for materials should be addressed to Michael Schüler.

**Peer review information** *Communications Physics* thanks the anonymous reviewers for their contribution to the peer review of this work. Peer reviewer reports are available.

**Reprints and permission information** is available at <http://www.nature.com/reprints>

**Publisher's note** Springer Nature remains neutral with regard to jurisdictional claims in published maps and institutional affiliations.



**Open Access** This article is licensed under a Creative Commons Attribution 4.0 International License, which permits use, sharing, adaptation, distribution and reproduction in any medium or format, as long as you give appropriate credit to the original author(s) and the source, provide a link to the Creative Commons license, and indicate if changes were made. The images or other third party material in this article are included in the article's Creative Commons license, unless indicated otherwise in a credit line to the material. If material is not included in the article's Creative Commons license and your intended use is not permitted by statutory regulation or exceeds the permitted use, you will need to obtain permission directly from the copyright holder. To view a copy of this license, visit <http://creativecommons.org/licenses/by/4.0/>.

© The Author(s) 2022